Spatiotemporal dynamics of Coulomb-correlated carriers in semiconductors

F. Lengers,[1] R. Rosati,[2] T. Kuhn,[1] and D. E. Reiter[1]
[1]*Institut für Festkörpertheorie, Universität Münster, Wilhelm-Klemm-Strasse 10, 48149 Münster, Germany*
[2]*Department of Physics, Chalmers University of Technology, 412 96 Gothenburg, Sweden*

(Received 1 March 2019; published 25 April 2019)

When the excitation of carriers in real space is focused down to the nanometer scale, the carrier system can no longer be viewed as homogeneous, and ultrafast transport of the excited carrier wave packets occurs. In state-of-the-art semiconductor structures such as low-dimensional heterostructures or monolayers of transition-metal dichalcogenides, the Coulomb interaction between excited carriers becomes stronger due to confinement or reduced screening. This demands a fundamental understanding of strongly interacting electrons and holes and the influence of Coulomb correlations. To study the corresponding particle dynamics in a controlled way, we consider a system of up to two electron-hole pairs exactly within a wave-function approach. We show that the excited wave packets contain a nontrivial mixture of free-particle and excitonic states. We further scrutinize the influence of the Coulomb interaction on the wave-packet dynamics, revealing its different role for below- and above-band-gap excitation.

DOI: 10.1103/PhysRevB.99.155306

I. INTRODUCTION

Research of exciton-based devices is a growing field due to the promising aspect of direct interconnection of electronic signal processing and optical communication [1–5]. At the heart of most of these devices is the ultrafast motion of photoexcited electrons and holes within the semiconductor accessible by various experimental techniques [2,6,7]. The Coulomb interaction between electrons and holes in such devices is becoming more decisive, because in state-of-the-art semiconductor structures such as low-dimensional heterostructures or monolayers of transition-metal dichalcogenides, the Coulomb interaction is enhanced due to the confinement, and excitonic effects are becoming more pronounced. Exciton physics has additionally been boosted by the discovery of strongly bound excitons in monolayers of transition-metal dichalcogenides [8–11], and recently the spatiotemporal dynamics of these strongly bound excitons has been explored [12–14]. Therefore, it is of crucial importance to understand the impact of the Coulomb interaction on the ultrafast localized excitation and dynamics of interacting carrier wave packets. Such localized excitation can then be used to investigate fundamental processes such as charge transfer and capture processes, which naturally occur on nanometric scales. In this paper, we give a detailed view of this aspect in an exact description of the correlated carrier dynamics.

In view of nanometric length scales and ultrashort time scales, we are entering scales where semiclassical descriptions are not able to properly describe physical processes [15]. While the ultrafast carrier dynamics including coherent and incoherent excitons has been extensively studied for homogeneous excitations [16–19], inhomogeneous treatments are more complicated. The aspect of spatiotemporal dynamics of photoexcited carriers on ultrashort time and length scales has been studied either in the limit of low densities where Hartree-Fock approximations are applicable [20–25], or in the limit of an exact number of carriers taken as an initial condition [26,27]. While the treatment of the low-density case revealed the dynamics of the carrier excitation and the fundamental carrier and polarization transport after excitation, the latter underlines the effects of carrier correlations leading to strong deviations from the free-carrier behavior when treating correlated particles. Here, we use a theory based on a wave-function approach. By restricting ourselves to excitations of up to two electron-hole pairs, we are able to treat the carrier system and their Coulomb correlations exactly. We further account for the interaction of carriers with a strongly localized light field. In our model, we observe the transition between free-carrier transport and correlated carrier transport. To study a computationally feasible problem, which at the same time exhibits strong Coulomb effects, we use an optically excited one-dimensional (1D) semiconductor quantum wire as sketched in Fig. 1.

The paper is organized as follows: In Sec. II we define the Hamiltonian describing the carrier system including Coulomb- and light-field interaction. With this we set up our wave-function ansatz as well as the equations of motion. In Sec. III A we consider a low-intensity excitation both below and above the band gap. In Sec. III B we then increase the excitation power and accordingly the mean number of carriers, resulting in a different dynamics. To evaluate the influence of the excitons, in Sec. IV we analyze the results in the excitonic picture interpolating between low and high excitation. We finish with conclusions in Sec. V.

II. THEORY

A. Hamiltonian

As a system we assume a CdTe quantum wire with a 100 nm^2 cross section as sketched in Fig. 1. We restrict ourselves to the lowest carrier subbands, i.e., one conduction and

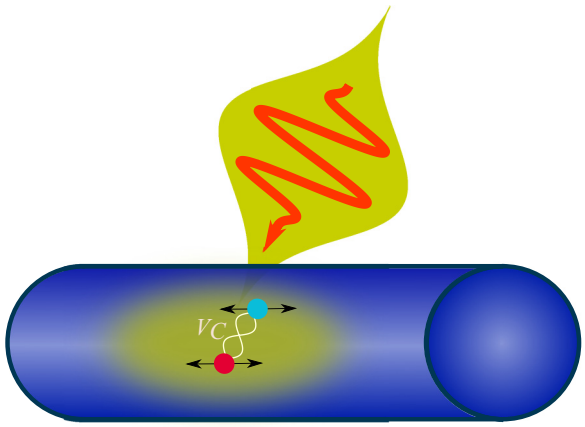

FIG. 1. Sketch of localized photoexcitation of a quantum wire resulting in traveling electron-hole pairs coupled via the Coulomb interaction V_C.

one valence band, which we assume to be spin-degenerate. The Hamiltonian of the noninteracting system is described by

$$\hat{H}_0 = \sum_{k,\sigma} \epsilon_k^e \hat{c}_{k\sigma}^\dagger \hat{c}_{k\sigma} + \sum_{k,\sigma} \epsilon_k^h \hat{d}_{k\sigma}^\dagger \hat{d}_{k\sigma},$$

with $\hat{c}_{k\sigma}$ ($\hat{c}_{k\sigma}^\dagger$) being the electron and $\hat{d}_{k\sigma}$ ($\hat{d}_{k\sigma}^\dagger$) the hole annihilation (creation) operators of a state with spin σ ($= \pm 1/2$) and longitudinal wave vector k; the energies are $\epsilon_k^e = E_{\mathrm{gap}} + \frac{\hbar^2}{2m_e}k^2$ and $\epsilon_k^h = \frac{\hbar^2}{2m_h}k^2$ with the effective masses $m_e = 0.091m_0$ and $m_h = 0.41m_0$ (m_0 being the free-electron mass) [28].

The system is excited by a linearly polarized localized laser pulse. The carrier-light-field interaction in the dipole approximation reads

$$\hat{H}_{\mathrm{cf}} = -\sum_{\substack{k,k'\\ \sigma}} [E_{k',k}\hat{c}_{k'\sigma}^\dagger \hat{d}_{-k\bar{\sigma}}^\dagger + \mathrm{c.c.}],$$

where $E_{k',k}(t) = \tilde{\mathbf{E}}(k-k',t)\cdot\mathbf{M}_{k',k}$ is the spatial Fourier transform of the electric-field amplitude $\mathbf{E}(z,t)$ multiplied by the interband dipole matrix element $\mathbf{M}_{k',k}$, which is assumed to be independent of k. Due to linear polarization, the dipole matrix element can be taken as independent of spin, and spin is conserved with $\bar{\sigma} = -\sigma$.

The Coulomb interaction in our system is [15]

$$\hat{H}_C = \frac{1}{2}\sum_{\substack{k,k',q\\ \sigma,\sigma'}} V_q [\hat{c}_{k\sigma}^\dagger \hat{c}_{k'\sigma'}^\dagger \hat{c}_{k'+q\sigma'}\hat{c}_{k-q\sigma} + \hat{d}_{k\sigma}^\dagger \hat{d}_{k'\sigma'}^\dagger \hat{d}_{k'+q\sigma'}\hat{d}_{k-q\sigma} - 2\hat{c}_{k\sigma}^\dagger \hat{d}_{k'\sigma'}^\dagger \hat{d}_{k'+q\sigma'}\hat{c}_{k-q\sigma}].$$

The first (second) term describes the electron-electron (hole-hole) interaction, while the third term is the attractive electron-hole interaction, which eventually will give rise to excitonic effects. For the Coulomb matrix element V_q, we use the bulk matrix element with static dielectric constant $\epsilon_s = 10.5$ multiplied by the quantum-wire form factor [21].

B. Equations of motion

The excitation of the quantum wire should be such that only up to two electron-hole pairs can be excited. This allows us to scrutinize the effects of the Coulomb interaction using a well-defined wave-function ansatz

$$|\Psi\rangle = a^{(0)}|0\rangle + \sum_{\substack{k,k'\\ \sigma,\sigma'}} a^{(1)}_{\substack{k,k'\\ \sigma,\sigma'}} \hat{c}_{k\sigma}^\dagger \hat{d}_{k'\sigma'}^\dagger |0\rangle + \sum_{\substack{k_1,k_2,k_3,k_4\\ \sigma_1,\sigma_2,\sigma_3,\sigma_4}} a^{(2)}_{\substack{k_1,k_2,k_3,k_4\\ \sigma_1,\sigma_2,\sigma_3,\sigma_4}} \hat{c}_{k_1\sigma_1}^\dagger \hat{c}_{k_2\sigma_2}^\dagger \hat{d}_{k_3\sigma_3}^\dagger \hat{d}_{k_4\sigma_4}^\dagger |0\rangle. \quad (1)$$

This wave function describes a state composed of one and two electron-hole pairs and the electron-hole vacuum $|0\rangle$ via the wave-function coefficients $a^{(0)}, a^{(1)}, a^{(2)}$. The validity of our approach can be tuned by the laser power and pulse duration since these parameters control the amount of excited carriers. Note that consistent with an initially undoped semiconductor, we assume electron-hole symmetry. This ansatz corresponds to a configuration-interaction (CI) approach often used in quantum chemistry for ground-state calculations of N-electron systems, although with our excitation-controlled electron-hole density we circumvent the usual problems of a truncated CI treatment [29,30]. Remarks on the comparison of the dynamical CI treatment and density-matrix approaches are given in Appendix A.

Next, we set up the equations of motion for the wave-function coefficients $a^{(0)}, a^{(1)}, a^{(2)}$ using the Schrödinger equation

$$i\hbar\frac{d}{dt}|\Psi\rangle = \hat{H}|\Psi\rangle.$$

Inserting the wave-function ansatz, commuting the fermionic annihilation operators to the right, and multiplying from the left with a zero-, one-, or two-pair state ($\langle 0|$, $\langle 0|\hat{d}_1\hat{c}_2$, or $\langle 0|\hat{d}_1\hat{d}_2\hat{c}_3\hat{c}_4$) leads then to the equations of motion, where the indices refer to the combination of wave vector and spin. To illustrate the occurring expectation values, we evaluate the most complicated expectation value as an example:

$$\begin{aligned}\langle 0|\hat{d}_1\hat{d}_2\hat{c}_3\hat{c}_4\hat{c}_\alpha^\dagger\hat{c}_\beta^\dagger\hat{d}_\gamma^\dagger\hat{d}_\delta^\dagger|0\rangle &= \delta_{\alpha,4}\delta_{\beta,3}(\delta_{\gamma,2}\delta_{\delta,1} - \delta_{\gamma,1}\delta_{\delta,2}) \\ &\quad - \delta_{\alpha,3}\delta_{\beta,4}(\delta_{\gamma,2}\delta_{\delta,1} - \delta_{\gamma,1}\delta_{\delta,2}). \quad (2)\end{aligned}$$

The δ-expressions give the same coefficients of the wave function because of the fermionic-induced symmetries,

$$a^{(2)}_{1234} = -a^{(2)}_{2134} = a^{(2)}_{2143} = -a^{(2)}_{1243}.$$

Due to the spin conservation, only coefficients with an equal number of up and down spins can occur. We therefore define

$$a^{(2)}_{\sigma,\sigma,\bar{\sigma},\bar{\sigma}} =: a^{(2),P}, \quad (3)$$

$$a^{(2)}_{\sigma,\bar{\sigma},\bar{\sigma},\sigma} =: a^{(2),A}, \quad (4)$$

which are the coefficients for parallel [$a^{(2),P}$ describing electrons (holes) with the same spin] and antiparallel [$a^{(2),A}$ describing electrons (holes) with different spin] carrier states. Further identifying

$$a^{(1)}_{\sigma_1,\sigma_2} =: a^{(1)}\delta_{\sigma_2,\bar{\sigma}_1}, \quad (5)$$

we may drop all spin indices in the following.

The equation of motion for the zero-pair coefficient reads

$$i\hbar\frac{d}{dt}a^{(0)} = -2\sum_{k,k'} E^*_{-k',k}a^{(1)}_{k,k'},$$

showing that only the coupling to a one-pair coefficient due to an electric field results in a change of $a^{(0)}$.

The equation for the one-pair coefficients is

$$i\hbar\frac{d}{dt}a^{(1)}_{k,k'} = \left(\epsilon^e_k + \epsilon^h_{k'}\right)a^{(1)}_{k,k'} - \sum_q V_q a^{(1)}_{k-q,k'+q} - E_{-k',k}a^{(0)} + 4\sum_{k_1,k_2}\left[E^*_{-k_2,k_1}\left(a^{(2),P}_{k,k_1,k',k_2} + a^{(2),A}_{k,k_1,k',k_2}\right)\right].$$

The first two terms on the right-hand side describe the excitonic dynamics, noting that for $k' = -k$ they resemble the Wannier equation for direct excitons. The third and the last two terms are source terms resulting from the coupling to zero pairs and to two pairs, respectively. The prefactor 4 of the last sum stems from the fermionic commutation relations.

The equation of motion for the two-pair coefficients $a^{(2),i}$ ($i = A, P$) is

$$\begin{aligned} i\hbar\frac{d}{dt}a^{(2),i}_{k_1,k_2,k_3,k_4} = &\left[\epsilon^e_{k_1} + \epsilon^e_{k_2} + \epsilon^h_{k_3} + \epsilon^h_{k_4}\right]a^{(2),i}_{k_1,k_2,k_3,k_4} + \frac{1}{4}E_{-k_4,k_2}a^{(1)}_{k_1,k_3} - \delta_{i,P}\frac{1}{4}E_{-k_3,k_2}a^{(1)}_{k_1,k_4} - \delta_{i,P}\frac{1}{4}E_{-k_4,k_1}a^{(1)}_{k_2,k_3} \\ &+ \frac{1}{4}E_{-k_3,k_1}a^{(1)}_{k_2,k_4} + \sum_q V_q\left[a^{(2),i}_{k_1-q,k_2+q,k_3,k_4} + a^{(2),i}_{k_1,k_2,k_3-q,k_4+q} - a^{(2),i}_{k_1-q,k_2,k_3+q,k_4}\right. \\ &\left. - a^{(2),i}_{k_1,k_2-q,k_3+q,k_4} - a^{(2),i}_{k_1-q,k_2,k_3,k_4+q} - a^{(2),i}_{k_1,k_2-q,k_3,k_4+q}\right]. \end{aligned}$$

In this equation, the dynamics of the two-pair exciton (or biexciton) is given by the first term and the last six terms, while the rest describe the excitation from the one-pair exciton. We note that the equations of motion for $a^{(0)}$ and $a^{(1)}$ are exact, while in principle in the equation of motion for $a^{(2)}$ we would have a source term stemming from $a^{(3)}$. Because we have restricted ourselves to two electron-hole pairs at most, this source term vanishes in our considerations.

The equations of motion are then solved by numerical integration with the initial condition of $a^{(0)} = 1$ and $a^{(1)} = a^{(2)} = 0$ discretized on a k-space grid with 60 points.

C. Dynamical quantities

The spatiotemporal dynamics of the excited carriers is encoded in the space-dependent density $n_{e/h}(z)$ for electrons and holes given by

$$n_e(z) = \langle\hat{n}_e(z)\rangle = \frac{1}{V}\sum_{k,k',\sigma}\langle\hat{c}^\dagger_{k\sigma}\hat{c}_{k'\sigma}\rangle e^{i(k'-k)z} \tag{6}$$

and the analogous definition for holes. Here z is the longitudinal position, and the factor 2 stems from the spin degeneracy due to linear polarization of the exciting electric field. The expectation value for electrons is given by

$$\begin{aligned}\langle\hat{c}^\dagger_{k\sigma}\hat{c}_{k'\sigma}\rangle = &\sum_{k_1} a^{(1)}_{k',k_1}a^{(1)*}_{k,k_1} + \sum_{k_1,k_2,k_3} 4\left[2a^{(2),P}_{k_1,k',k_2,k_3}a^{(2),P*}_{k_1,k,k_2,k_3}\right. \\ &\left. + 4a^{(2),A}_{k',k_1,k_3,k_2}a^{(2),A*}_{k,k_1,k_3,k_2}\right],\end{aligned}$$

being independent of spin and analogous for the holes.

To further analyze the dynamical behavior of the energies in the system, we define the kinetic energies for electrons and holes,

$$E^e_{\rm kin} = \sum_{k,\sigma}\left(\epsilon^e_k - E_{\rm gap}\right)\langle\hat{c}^\dagger_{k\sigma}\hat{c}_{k\sigma}\rangle, \quad E^h_{\rm kin} = \sum_{k,\sigma}\epsilon^h_k\langle\hat{d}^\dagger_{k\sigma}\hat{d}_{k\sigma}\rangle,$$

and the interaction energy

$$\begin{aligned}E_{\rm int} = \frac{1}{2}\sum_{\substack{k,k',q\\ \sigma,\sigma'}} V_q[&\langle\hat{c}^\dagger_{k\sigma}\hat{c}^\dagger_{k'\sigma'}\hat{c}_{k'+q\sigma'}\hat{c}_{k-q\sigma}\rangle \\ &+ \langle\hat{d}^\dagger_{k\sigma}\hat{d}^\dagger_{k'\sigma'}\hat{d}_{k'+q\sigma'}\hat{d}_{k-q\sigma}\rangle - 2\langle\hat{c}^\dagger_{k\sigma}\hat{d}^\dagger_{k'\sigma'}\hat{d}_{k'+q\sigma'}\hat{c}_{k-q\sigma}\rangle].\end{aligned}$$

The interaction energy can be further divided into the Hartree-Fock energy and the correlation energy. The Hartree-Fock energy is calculated by factorizing the two-particle into one-particle density matrices [15],

$$\begin{aligned}E_{\rm HF} = \sum_{k,k',q} V_q\big[&2f^e_{k',k'+q}f^e_{k,k-q} - f^e_{k,k'+q}f^e_{k',k-q} \\ &+ 2f^h_{k',k'+q}f^h_{k,k-q} - f^h_{k,k'+q}f^h_{k',k-q} \\ &- 4f^e_{k',k'+q}f^h_{k,k-q} - 2p^*_{k'+q,k}p_{k',k-q}\big],\end{aligned}$$

where f^i are the electron (hole) intraband coherences for $i = e$ ($i = h$), and p are the interband polarizations (see Appendix A). With this we define the correlation energy as

$$E_{\rm cor} = E_{\rm int} - E_{\rm HF}. \tag{7}$$

This quantity gives us a direct measure for the correlation of the system. The correlations thereby describe the effects beyond simple electrostatic and exchange Coulomb interactions of carriers.

We remark that all energies shown in the following are normalized to the final mean number of electrons $N_e = 2\sum_k\langle\hat{c}^\dagger_k\hat{c}_k\rangle$.

III. RESULTS

We now consider the dynamics of the optically generated carriers within the quantum wire. For the excitation we consider a pulse that is Gaussian in both space and time. We

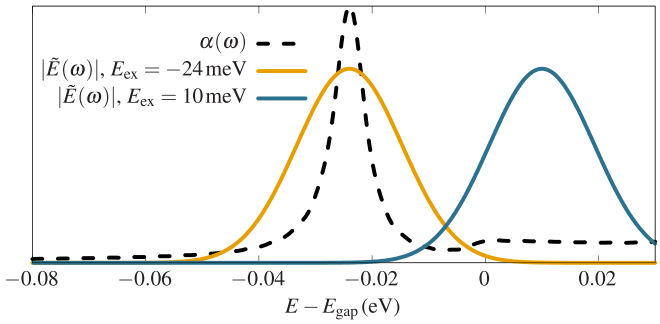

FIG. 2. Linear absorption spectrum (dashed line) and spectrum (solid lines) of the exciting laser pulses with different excess energy E_{ex}.

set the spatial variance of the pulse to 10 nm, corresponding to a full width at half-maximum FWHM ≈ 23.5 nm. The pulse duration is set to 100 fs. Additional parameters are the excitation energy $\hbar\omega_L$ and the intensity, which we will vary in the following.

Our system can be characterized by its absorption spectrum $\alpha(\omega)$ as shown in Fig. 2, where a phenomenological dephasing time of 250 fs was added. The absorption spectrum can be divided into two parts, namely the excitonic resonance at -24 meV below the band gap E_{gap} and the continuum states for energies above the band gap $E > E_{gap}$. In the following, we will consider two distinct excitation energies: (i) an excitation at the exciton resonance below the band gap, i.e., laser excess energy $E_{ex} = \hbar\omega_L - E_{gap} = -24$ meV, and (ii) an excitation into the continuum states with a laser excess energy $E_{ex} = 10$ meV. The corresponding laser pulse spectra are marked in Fig. 2 with the excitonic excitation at $E_{ex} = -24$ meV as an orange line and the continuum excitation with $E_{ex} = 10$ meV as a blue line.

These two excitation conditions for low excitation strength will result in the excitation of either exclusively excitons or free carriers, respectively. For increasing field strength, we increase the particle number and we expect that Coulomb correlations will become important. Therefore, the excitation strength will be our tuning knob.

A. Low-density limit

We start by looking at an excitation with a low laser power, such that the total number of electrons after the pulse is $N_e \approx 10^{-4}$, which we refer to as the low-density limit. In Fig. 3 we plot the dynamics of electron (left) and hole (right) densities for an excitation (a) below and (b) above the band gap.

When exciting the system at the exciton resonance [Fig. 3(a)], we find an electron-hole pair at $z = 0$ with almost no spatial dynamics. Here electrons and holes are bound by the Coulomb interaction in the $1s$ exciton without any center-of-mass momentum. In contrast, when exciting within the continuum [Fig. 3(b)], independent electron and hole wave packets are excited that travel along the wire. Their velocity is dictated by the excess energy according to $v_e = \frac{\hbar k_0}{m_e}$ ($v_h = \frac{\hbar k_0}{m_h}$) for electrons (holes), where $k_0 = \sqrt{2\mu E_{ex}}/\hbar$, $\mu^{-1} = m_e^{-1} + m_h^{-1}$ being the reduced mass. Therefore, the holes travel much slower and due to the low density the carrier wave packets

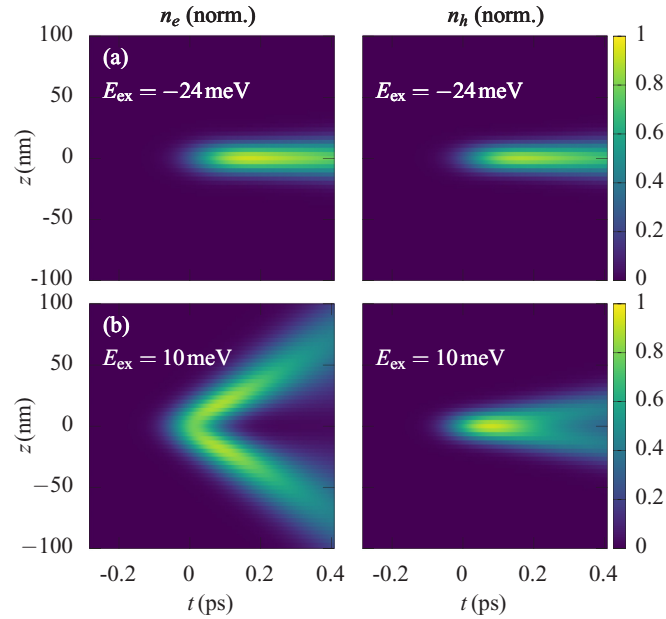

FIG. 3. Dynamics of the electron (left) and hole (right) density $n_{e/h}$ in the low-density limit for an excitation (a) resonant to the $1s$ exciton and (b) within the continuum. All the distributions have been normalized to their respective maxima.

do not affect each other. Our results in the low-density limit agree well with calculations for excitation in semiconductor quantum wells [20].

In Fig. 4 we study the energy contributions normalized to the final electron number for the two excitation conditions to get more insight into the Coulomb effects. For the excitation of the exciton, given in Fig. 4(a), we find that E_{tot} (red line) is close to the binding energy of the $1s$ exciton, underlining the fact that a bound electron-hole pair is excited. The kinetic energies for electrons and holes (black lines) have small values compared to the total energy. The strong influence of the Coulomb interaction is also seen in the interaction energy

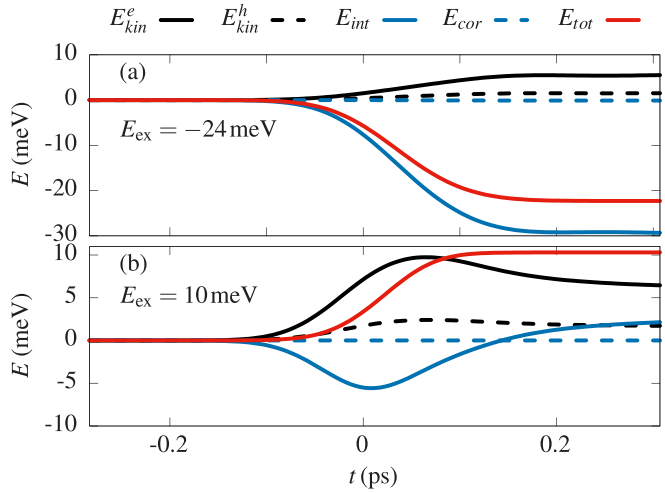

FIG. 4. Energy contributions normalized to the final electron number for an excitation (a) resonant to the exciton and (b) within the continuum.

E_{int} (blue line), which is much stronger than the kinetic ones. The interaction energy mostly describes coherent excitons, which are well-described in a Hartree-Fock picture and, accordingly, the correlation energy E_{cor} vanishes. This leads to the conclusion that a Hartree-Fock picture is applicable, in which only coherent excitons are present, in agreement with the low-density limit. In this limit, the dynamics is still linear in the electric field E and all many-particle quantities factorize like

$$\langle \hat{c}_1^\dagger \hat{d}_2^\dagger \hat{d}_3 \hat{c}_4 \rangle = \langle \hat{c}_1^\dagger \hat{d}_2^\dagger \rangle \langle \hat{d}_3 \hat{c}_4 \rangle + \langle \hat{c}_1^\dagger \hat{c}_4 \rangle \langle \hat{d}_2^\dagger \hat{d}_3 \rangle + O(E^4).$$

Here the first term on the right-hand side is of order E^2 and already the second term is of order E^4 [31].

The energies in the case of continuum excitation, displayed in Fig. 4(b), are rather different. Note the different scales of Figs. 4(a) and 4(b). The total energy approaches the excess energy of the exciting laser pulse, while the kinetic energies are similar to the below-band-gap excitation. The main difference lies in the interaction energy, which starts off with negative values, showing that, even though we excited the system within the continuum, the Coulomb interaction alters the carrier dynamics directly above the band gap, in particular during the laser pulse. After the laser pulse, the interaction energy approaches a small positive value one order of magnitude smaller than the interaction energy in Fig. 4(a). If one increases the excess energy even further, a gradual decrease of the interaction energy occurs (not shown). Again, due to the low-density limit, the correlation energy vanishes.

B. High-density limit

We will now turn to higher excited densities ($1 \leqslant N_e \leqslant 2$) in which the electron and hole wave packets should interact strongly with each other. We will refer to this as the high-density limit. While in the low-density case one could describe the $E_{\text{ex}} = -24$ and 10 meV cases by excitonic and free-carrier excitation, respectively, in a high-density case we expect a more complex picture, because the former interpretations rely on low-density eigenstates of the semiconductor.

1. Excitonic excitation

Starting with the excitation at the exciton resonance, we increase the pulse strength, such that on average $N_e \approx 1.7$ electrons are excited. The corresponding density dynamics and energy contributions are shown in Fig. 5. We again see that the density is strongly localized at $z = 0$ with little movement. Comparing the densities in the high-density [Fig. 5(a)] and low-density case [Fig. 3(a)], one observes an increased broadening of the carrier densities with time, which will be further quantified below. The increased broadening of the carrier densities can be understood in terms of Coulomb scattering processes, which broaden the momentum distribution. Even though Markovian Coulomb-induced intraband scattering does not exist in a 1D system, on the ultrafast timescales considered here quantum kinetic Coulomb scattering can strongly affect the carrier distributions [32].

Figure 5(b) shows the energy contributions. Comparing the energetic contributions with the energy contributions in the low-density case [Fig. 4(a)], one surprisingly sees that most energies do not change considerably. Only the correlation

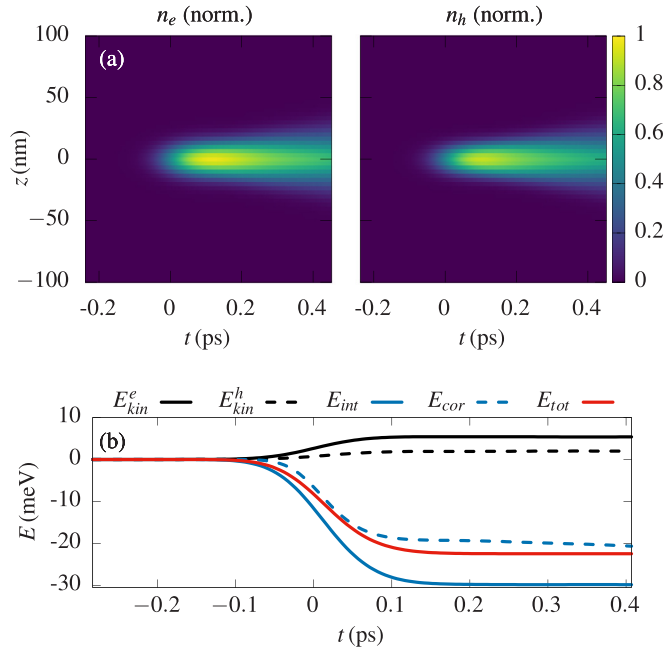

FIG. 5. Spatiotemporal carrier dynamics in the high-density case after a 100 fs pulse with excess energy $E_{\text{ex}} = -24$ meV. (a) Dynamics of electron and hole distributions and (b) energy contributions.

energy is now dominating the interaction energy, which shows that the carrier interaction is now dominated by correlations beyond the Hartree-Fock picture. Nevertheless, it is still reasonable to say that the carriers are still in a bound state with $E_{\text{tot}} \approx -22$ meV. A direct comparison of the spatiotemporal dynamics with a pure Hartree-Fock treatment is presented in Appendix A.

Concerning the spatial broadening of the carrier densities, the interesting question arises whether the transport is still ballistic in view of the time and length scales or already diffusive in view of scattering mechanisms. To answer this question, we calculate the variance of the distribution

$$\Delta z_i^2 = \frac{1}{N_i(t)} \int z^2 n_i(z) dz,$$

where $N_i(t)$ $(i = e, h)$ is the number of excited particles at time t. The power dependence of $\Delta z_i^2 \propto t^m$ is then an indicator for the transport regime, where $m = 1$ corresponds to diffusion and $m = 2$ to ballistic motion [33]. The variance of the electronic density for the two pulse intensities is shown in Fig. 6. For both excitation regimes one can clearly see the dependence $\Delta z_i^2 \propto t^2$, which is confirmed by fits (black dashed lines). Therefore, we conclude that the transport is still ballistic (the hole variance shows the same scaling and is therefore not shown here). Nevertheless, one can observe a huge increase in ballistic broadening with increased density due to Coulomb correlations; note that a quantum-mechanical speed-up of the ballistic broadening has also been observed as a result of other scattering mechanisms [34]. This behavior can also be understood by the fact that for elevated densities, the excited carriers are no longer described by a completely excitonic excitation, but by an admixture of continuum excitations that are spatially less bound (see also Sec. IV).

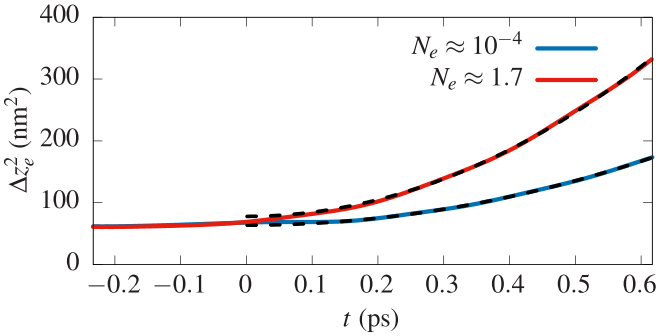

FIG. 6. Variance of the electronic wave packet as a function of time for the low-intensity ($N_e \approx 10^{-4}$, blue line) and high-intensity ($N_e \approx 1.7$, red line) case. The black dashed lines indicate quadratic fits $\propto t^2$ to the respective curves.

2. Continuum excitation

We now consider the case of continuum excitation in the high-density limit for an excitation with a pulse strength, such that $N_e \approx 1.7$. The corresponding dynamics of the densities is shown in Fig. 7(a). For both electrons and holes, we find that wave packets are excited, which travel along the wire. In contrast to the low-intensity limit [Fig. 3(b)], now a strong spatial spreading of the densities and an acceleration of the hole wave packet is found.

When looking at the corresponding energies, shown in Fig. 7(b), the acceleration of holes is directly visible in the kinetic energy E^h_{kin}, which now is on the same level as the kinetic energy of electrons E^e_{kin}. The increase in kinetic energy is compensated by a strong negative interaction energy E_{int}, which for high densities is dominated by the correlation

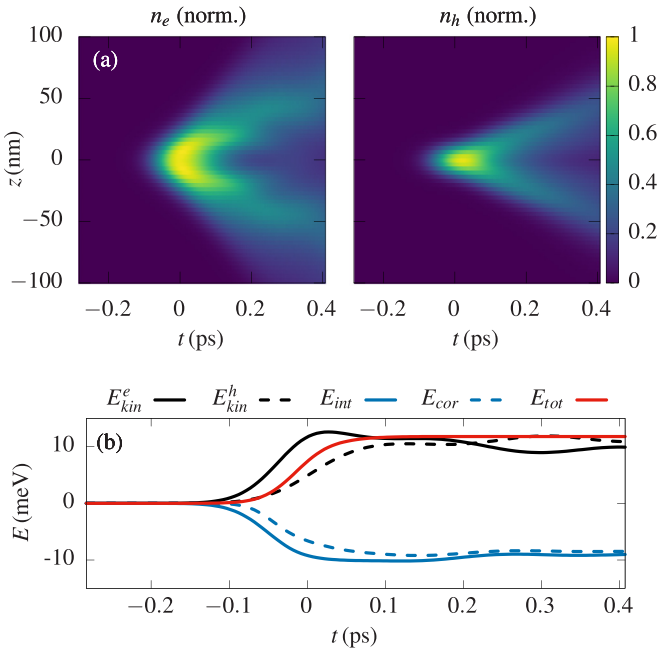

FIG. 7. Spatiotemporal carrier dynamics after a 100 fs pulse with excess energy $E_{\text{ex}} = 10$ meV. (a) Dynamics of electron and hole distributions and (b) energy contributions.

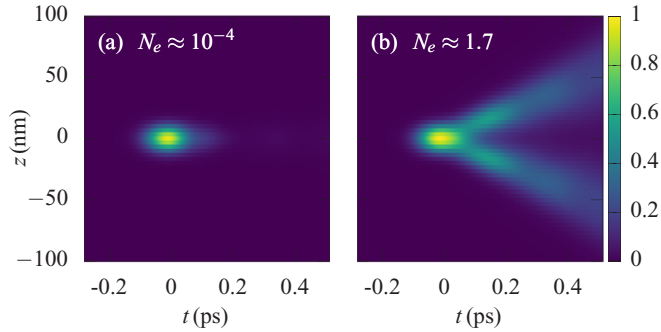

FIG. 8. Normalized two-particle density [cf. Eq. (8)] for continuum excitation in (a) the low-density limit and (b) the high-density limit.

energy, such that the total energy is only slightly changed in comparison to the low-density case.

Let us discuss in some more detail the strong acceleration of holes, which is the most striking difference from the low-density case. The holes are accelerated such that they travel with approximately the same velocity as the electrons. This can already be explained on a Hartree-Fock level where the strong charge density induced by the local excitation leads to a strong electrostatic interaction of the wave packets ultimately forming an ambipolar wave packet effectively reducing the charge density (see Appendix A for a Hartree-Fock simulation). The formation of an ambipolar wave packet as in the present case, where electrons and holes are moving with approximately the same velocity, can be directly mapped by the two-particle density with equal electron and hole positions,

$$N_{2P}(z) = \sum_{\sigma} \left\langle \hat{\Psi}^{\dagger e}_{\sigma}(z) \hat{\Psi}^{\dagger h}_{\bar{\sigma}}(z) \hat{\Psi}^{h}_{\bar{\sigma}}(z) \hat{\Psi}^{e}_{\sigma}(z) \right\rangle$$
$$= \frac{1}{V^2} \sum_{\substack{k,k',\sigma \\ K,K'}} e^{i(K-K')z} \left\langle \hat{c}^{\dagger}_{k'+\frac{K'}{2}\sigma} \hat{d}^{\dagger}_{-k'+\frac{K'}{2}\bar{\sigma}} \hat{d}_{-k+\frac{K}{2}\bar{\sigma}} \hat{c}_{k+\frac{K}{2}\sigma} \right\rangle, \tag{8}$$

where $\hat{\Psi}^{\dagger i}_{\sigma}(z)$ are the field operators creating a carrier i at position z. Here k, k' describe the relative momenta and K, K' are the center-of-mass momenta of the carriers. We plot the two-particle density of Eq. (8) for the low- and high-density limit in Fig. 8, which should be compared to the densities shown in Figs. 3(b) and 7(a), respectively. In the low-density limit [Fig. 8(a)], a fast temporal decay of the two-particle density is visible because of the spatial separation of electron and hole wave packets.

In contrast, in the case of high density [Fig. 8(b)] one observes a traveling wave packet tracking the motion of carriers directly reflecting the formation of the ambipolar wave packet. Another quantification of the acceleration of holes can be gained from the dynamics of the carrier occupations $f^e(\epsilon^e_k) = \langle \hat{c}^{\dagger}_k \hat{c}_k \rangle$, $f^h(\epsilon^h_k) = \langle \hat{d}^{\dagger}_k \hat{d}_k \rangle$ shown in Fig. 9 for (left panels) the low-density limit with $N_e \approx 10^{-4}$ and (right panels) the high-density limit with $N_e \approx 1.7$. In the low-density limit, we observe essentially an excitation at k-values corresponding to the excess energy $k_0 = \sqrt{2\mu E_{\text{ex}}}/\hbar$ ($\epsilon^e_{k_0} \approx E_{\text{ex}} > \epsilon^h_{k_0}$) distributed between electrons and holes. During the pulse, due to the

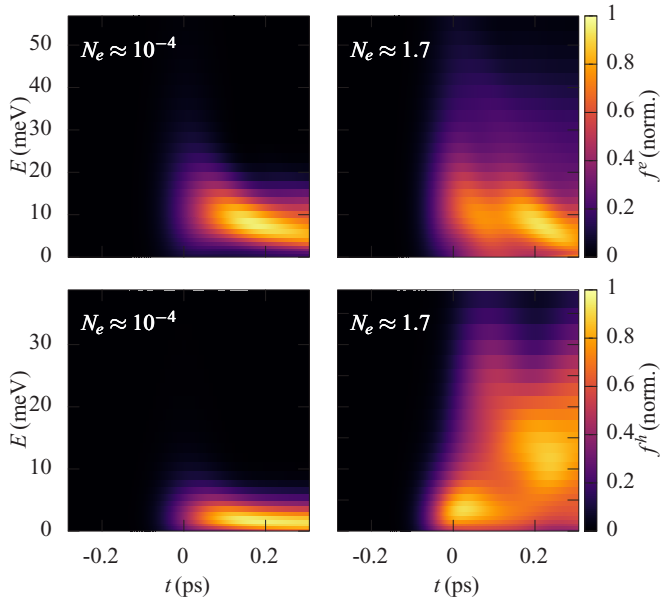

FIG. 9. Energy distribution of the carrier occupations $f^{e/h}$ as a function of time in the low- (left panels) and high-density limit (right panels).

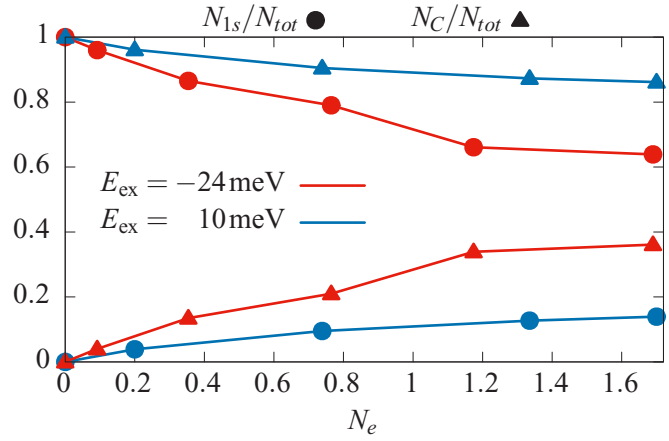

FIG. 10. Final excitonic (circles) and continuum (triangles) occupation probabilities for different carrier densities for $E_{ex} = -24$ meV (red symbols) and $E_{ex} = 10$ meV (blue symbols).

renormalization by Coulomb effects, the energy distribution is smeared out.

In contrast, when looking at the dynamics in the high-density case, the electronic distribution (upper panel) is mostly smeared out by correlation effects, and the hole distribution shows a strong acceleration from $E \approx 3$ meV to $E \approx 12$ meV, resulting in the acceleration of the hole wave packets observed in Fig. 7(a). Additionally, a strong broadening of the distribution is observed that is even stronger than in the case of electrons because the Coulomb scattering of holes is facilitated by their flatter band structure. The strong energetic broadening of the distributions leads to the enhanced spatial spreading, because a broader range of wave-packet velocities contributes to the wave packet.

IV. EXCITONIC PICTURE

To discriminate more clearly between the excitonic occupations and the continuum contributions for the different excitations, we now analyze our results using an excitonic picture. In this picture, all quantities are transformed into the two-particle picture defined by the excitonic eigenfunctions [17,35]. This will be particulary helpful for the high-density limit, where the distinction between exciton and continuum carriers becomes questionable. The exciton occupations can be defined as

$$\langle \hat{Y}_x^\dagger \hat{Y}_x \rangle := \sum_{q,q',\sigma} g^x_{q,K-q} \left(g^x_{q',K'-q'}\right)^* \langle \hat{c}^\dagger_{q\sigma} \hat{d}^\dagger_{K-q\bar{\sigma}} \hat{d}_{K-q'\bar{\sigma}} \hat{c}_{q'\sigma} \rangle,$$

with $x = (n, K)$ consisting of the center-of-mass momentum K and the hydrogenlike quantum number n ($1s, \ldots,$ continuum). $\hat{Y}_x$ ($\hat{Y}_x^\dagger$) is the exciton annihilation (creation) operator. The expansion coefficients $g^x_{q,K-q}$ describe the transformation from the free-particle states to the exciton states with the relative momentum q (see Appendix B). Having done that, we compute the fraction of $1s$ excitons and continuum excitons using

$$N^x_{\text{tot}} = \sum_x \langle \hat{Y}_x^\dagger \hat{Y}_x \rangle = N_{1s} + N_C,$$

with $N_{1s} = \sum_K \langle \hat{Y}^\dagger_{1s,K} \hat{Y}_{1s,K} \rangle$. Thereby, one can distinguish between excited bound electron-hole pairs and electron-hole pairs within the excitonic continuum, which essentially behave like independent particles. We consider here all states above the $1s$ states as a continuum, because higher excitonic states merge with the continuum excitations (cf. Fig. 2).

The stationary values of N_{1s} and N_C (normalized to the total number of two-pair states) at the end of the simulation ($t \approx 0.45$ ps) are shown in Fig. 10 as a function of the excitation power quantified by the number of electrons N_e. One can directly see that the behaviors for the two excess energies are opposed to each other. In the low-density case there are only excitonic carriers for $E_{ex} = -24$ meV (red symbols) and only continuum carriers for $E_{ex} = 10$ meV (blue symbols). For increasing densities, the excitonic and continuum carriers start to mix. For the excitonic excitation this is expected, because the excitonic resonance becomes screened for increased carrier densities. In the case of continuum excitation, the Coulomb interaction between the finite densities leads to the fact that the wave packets, which are initially of free-carrier character, interact with each other and thereby acquire an excitonic nature. It is worth noting that the mixing of continuum and excitonic carriers is more strongly influenced by the density for the excitonic excitation than for the continuum excitation, such that at $N_e \approx 1.7$ the carriers are only 60% excitonic.

We further look at the exciton occupations within the $1s$ band,

$$N_{1s}(E_C) = \left\langle \hat{Y}^\dagger_{1s,K(E_C)} \hat{Y}_{1s,K(E_C)} \right\rangle,$$

where E_C denotes the center-of-mass energy. The final distribution in the two excitation scenarios is shown in Fig. 11 for different excitation strengths denoted by the number of particles N_e. In Fig. 11(a) we consider the excitonic excitation. In the low-density limit, the width of the distribution (blue

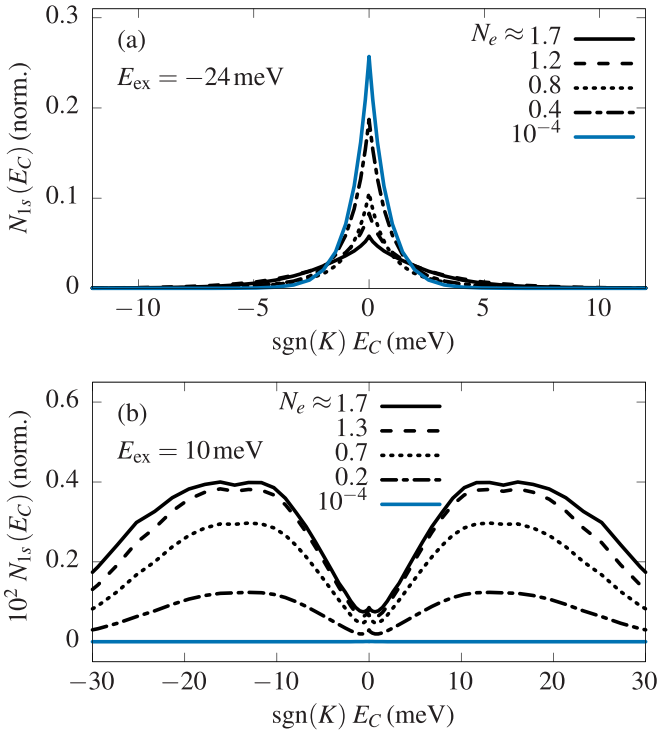

FIG. 11. Normalized $1s$ exciton distribution as a function of center-of-mass energy at the end of the simulation for (a) excitonic and (b) continuum excitation. The black solid line corresponds to the high-density limit and the blue solid line to the low-density limit.

line) is exclusively determined by the spatial localization of the exciting pulse. For increased intensity (increasing N_e), the distribution successively broadens such that a considerable fraction of excitons with finite center-of-mass momentum is present. This energetic broadening to higher center-of-mass energies is in agreement with the enhanced ballistic spreading for higher carrier densities together with the admixture of continuum carriers shown in Fig. 10. For the continuum excitation presented in Fig. 11(b), we find a much broader distribution to start with, which is centered around a finite center-of-mass energy representing the fact that moving ambipolar wave packets are traveling through the quantum wire. With increasing excitation strength the finite momentum successively builds up from the low-density limit, where the center-of-mass momentum is essentially zero and the $1s$ occupation is vanishing. Thereby, it is the acceleration of holes that leads to the fact that the absolute values of electron and hole momenta are not equal anymore, and excitonic occupations with finite center-of-mass momentum $K = k_e + k_h$ build up.

V. CONCLUSION

In summary, we have discussed the impact of Coulomb effects on the ultrafast spatiotemporal carrier dynamics in semiconductors. As an example, we have considered the dynamics in a semiconductor quantum wire. For this, we have performed calculations in a configuration-interaction-like approach. By restricting ourselves to at most two electron-hole pairs, we obtain an exact model ready to scrutinize the Coulomb effects and correlations beyond the Hartree-Fock level. This allowed us to examine the influence of the Coulomb interaction on the exciton dynamics in particular for different carrier densities. While in the low-density limit, where only a few carriers are excited, the exciton and continuum states could be well separated, for higher excitation density Coulomb correlations lead to a mixing of those.

These effects are also seen in the spatiotemporal dynamics of the excited carriers, which behave qualitatively differently in the low- and high-density limit. The excitation resonant to the exciton leads to mostly stationary carriers, which for higher density still move ballistically, but much faster away from the excitation region, resulting in ultrafast spatial spreading. For excitations in the continuum, two mostly independent electron and hole wave packets were formed traveling along the quantum wire. In contrast, for higher densities a strong acceleration of the hole wave packet led to the formation of an ambipolar wave packet. This wave packet can be dominantly characterized by carriers within the excitonic continuum and a fraction of excitons with finite center-of-mass momentum.

Our studies give important insights in the dynamics of excitons in low-dimensional semiconductors and will help in the development of exciton-based devices in semiconductor technology.

ACKNOWLEDGMENTS

F.L. and D.E.R. acknowledge financial support by the Deutsche Forschungsgemeinschaft (DFG) through the project 406251889 (RE 4183/2-1). We also thank V. M. Axt for fruitful discussions.

APPENDIX A: COMPARISON TO OTHER THEORETICAL TREATMENTS

Here, we briefly compare our wave-function-based CI approach to density matrix approaches, which are commonly used to treat photoexcited semiconductors [15,18] and—as a specific example—to a Hartree-Fock calculation.

We remark that our CI approach is able to describe quantities up to a biexciton occupation exactly, which is described by an eight-operator expectation value. In perturbative approaches, those expectation values are usually expanded in products of lower expectation values, and correlations of a certain order are neglected. While such a decoupling scheme can, e.g., be unambiguously truncated in finite orders of the electric field for nonlinear spectroscopy [31], it is hard to define a truncation scheme for high excitation densities, especially when only a few carriers are excited, i.e., for strong spatial localizations, where correlation effects should dominate. Mean-field treatments, such as the Hartree-Fock factorization, which are usually the basis of density-matrix approaches, are not justified in those cases. An additional advantage of the CI method in comparison to the aforementioned density matrix approaches is the fact that the evaluation of the Schrödinger equation will result in linear differential equations, which are numerically much more stable than the nonlinear equations of motion of a density-matrix-based decoupling scheme. The CI approach is therefore powerful in the context of strongly localized excitation since here only a few particles are present in the system and their correlation is of crucial importance.

Nevertheless it is mandatory that the number of particles is known and fixed throughout the simulation. This makes the treatment of effects like Auger-recombination or impact-ionization and the treatment of bosonic particles difficult.

It is interesting to directly compare our approach to a Hartree-Fock (HF) calculation. The equations of motion in this case read

$$\frac{d}{dt}f^e_{k,k'} = \frac{i}{\hbar}\sum_{k''}\left[\mathcal{E}^e_{k,k''}f^e_{k'',k'} - f^e_{k,k''}\mathcal{E}^e_{k'',k'}\right] - \frac{i}{\hbar}\sum_{k''}[\mathcal{U}^*_{k'',k}p_{k'',k'} - p^*_{k'',k}\mathcal{U}_{k'',k'}],$$

$$\frac{d}{dt}f^h_{k,k'} = \frac{i}{\hbar}\sum_{k''}\left[\mathcal{E}^h_{k,k''}f^h_{k'',k'} - f^h_{k,k''}\mathcal{E}^h_{k'',k'}\right] - \frac{i}{\hbar}\sum_{k''}[\mathcal{U}^*_{-k,-k''}p_{-k',-k''} - p^*_{-k,-k''}\mathcal{U}_{-k',-k''}],$$

$$\frac{d}{dt}p_{k,k'} = -\frac{i}{\hbar}\sum_{k''}\left[\mathcal{E}^h_{-k'',-k}p_{k'',k'} + p_{k,k''}\mathcal{E}^e_{k'',k'}\right] + \frac{i}{\hbar}\sum_{k''}\left[(\delta_{k'',k} - f^h_{-k'',-k})\mathcal{U}_{k'',k'} - \mathcal{U}_{k,k''}f^e_{k'',k'}\right],$$

with $f^e_{k,k'} = f^e_{k,k',\sigma} = \langle\hat{c}^\dagger_{k\sigma}\hat{c}_{k'\sigma}\rangle$, $f^h_{k,k'} = f^h_{k,k',\sigma} = \langle\hat{d}^\dagger_{k\sigma}\hat{d}_{k'\sigma}\rangle$, $p_{k,k'} = p_{k,k',\sigma} = \langle\hat{d}_{-k\bar{\sigma}}, \hat{c}_{k'\sigma}\rangle$, the renormalized energies

$$\mathcal{E}^{e/h}_{k,k'} = \epsilon^{e/h}_k\delta_{k,k'} - \sum_q V_q f^{e/h}_{k+q,k'+q} + 2V_{k-k'}\sum_q\left(f^{e/h}_{k+q,k'+q} - f^{h/e}_{k+q,k'+q}\right),$$

and the renormalized fields

$$\mathcal{U}_{k,k'} = E_{k,k'}(t) + \sum_q V_q p_{k+q,k'+q}$$

(see Ref. [15]). For this, we show the continuum excitation in the high-density limit for CI and Hartree-Fock in Fig. 12. The upper panel shows the Hartree-Fock calculations, and the lower one shows the CI calculations (these were already shown in Fig. 7 in Sec. III B 2). For both calculations one finds that electron and hole wave packets are formed, which travel along the wire with the same speed. In other words, the general trend of the formation of an ambipolar wave packet is already described on the Hartree-Fock level, underlining the interpretation that the driving force for this formation is the classical electrostatic attraction between electron and hole. Nevertheless the spatial broadening of the densities is underestimated on the Hartree-Fock level, because quantum kinetic scattering is not incorporated. For the same reason there is a density at $z = 0$ in Hartree-Fock building up after the pulse has ended, because the renormalized electric field does not dephase in the Hartree-Fock treatment. We conclude that the Hartree-Fock approximation gives a qualitatively correct prediction of the ambipolar wave packet and therefore might be a valid choice for dynamical calculations of wave packets.

Finally, we want to explore whether the ballistic nature of the transport in the case of the excitonic excitation is already captured in a Hartree-Fock calculation. Therefore, we show

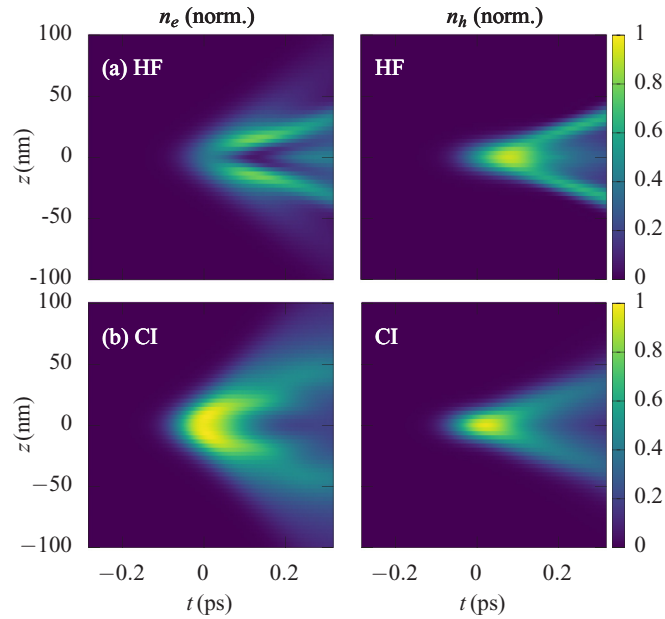

FIG. 12. Electronic (left column) and hole (right column) densities for continuum excitation in the high-density limit using (a) a Hartree-Fock (HF) simulation and (b) the wave-function-based CI simulation [cf. Fig 7(a)].

in Fig. 13 the dynamics of Δz_e^2 for an excitonic excitation, and we compare the CI simulation (see also Fig. 6) with the results from the Hartree-Fock calculation given in orange (dashed). The Hartree-Fock case strongly underestimates the spatial spreading of the wave packet and also falsely predicts a superballistic behavior with $\Delta z_e^2 \propto t^{3.2}$. Therefore, in this case the Hartree-Fock approximation fails to correctly describe the dynamical behavior of the exciton.

In summary, the comparison with a Hartree-Fock treatment underlines the fact that a correlation-expansion scheme is a valid method for systems in which energetic continua play a role, as in the case of continuum excitation. In the case of excitonic excitation there is the center-of-mass continuum, but nevertheless no continuum in relative coordinates.

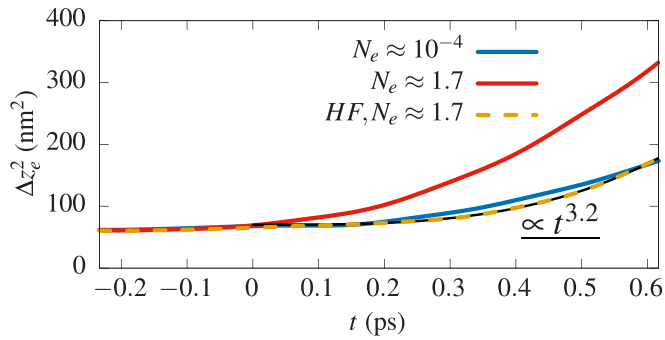

FIG. 13. Wave-packet variance Δz_e^2 as a function of time (cf. Fig. 6) now also including the Hartree-Fock simulation (orange dashed line). A polynomial fit is shown as a black solid line.

APPENDIX B: EXCITONIC EIGENSPACE

In this Appendix, we briefly summarize the transformation to the exciton eigenspace. We consider the ansatz for the excitonic eigenfunctions $|\varphi^x\rangle = \sum_{k_1,k_2} g^x_{k_1,k_2} \hat{c}^\dagger_{k_1\sigma_1} \hat{d}^\dagger_{k_2\sigma_2} |0\rangle$. This results in the Wannier equation

$$\sum_q \left[\left(\epsilon^e_{k_1} + \epsilon^h_{k_2}\right)\delta_{q,0} - V(q)\right] g^x_{k_1+q,k_2-q} = E_x g^x_{k_1,k_2}$$

after projecting the system Hamiltonian on $|\varphi^x\rangle$. The solution with $x = n, K$ reads

$$\begin{aligned} g^{n,K}_{k_1,k_2} &= \delta_{k_1+k_2,K}\tilde{\phi}_n\left(\frac{m_h}{M}k_1 - \frac{m_e}{M}k_2\right) \\ &= \delta_{k_2,K-k_1}\tilde{\phi}_n\left(k_1 - \frac{m_e}{M}K\right), \end{aligned}$$

$K = k_1 + k_2$ being the center-of-mass momentum of the exciton, $M = m_e + m_h$, and $\tilde{\phi}_n$ determined by the solution of the effective hydrogen problem,

$$\sum_q \left[\frac{\hbar^2 k^2}{2\mu}\delta_{q,0} - V(q)\right]\tilde{\phi}_n(k+q) = \epsilon_n \tilde{\phi}_n(k),$$

with the reduced mass $\mu = \frac{m_e m_h}{m_e + m_h}$.

Within this basis one can obtain, e.g., the excitonic polarization as

$$\begin{aligned} \hat{Y}^\dagger_{n,K} &= \sum_{k_1,k_2} g^{n,K}_{k_1,k_2} \hat{c}^\dagger_{k_1\sigma} \hat{d}^\dagger_{k_2\bar{\sigma}} \\ &= \sum_{k_1} \tilde{\phi}_n\left(k_1 - \frac{m_e}{M}K\right)\hat{c}^\dagger_{k_1\sigma}\hat{d}^\dagger_{K-k_1\bar{\sigma}}, \end{aligned}$$

where we defined the optically active excitonic state.

[1] C. Lienau, V. Emiliani, T. Guenther, F. Intonti, T. Elsaesser, R. Notzel, and K. Ploog, Phys. Status Solidi A **178**, 471 (2000).
[2] P. Vasa, C. Ropers, R. Pomraenke, and C. Lienau, Laser Photon. Rev. **3**, 483 (2009).
[3] A. A. High, E. E. Novitskaya, L. V. Butov, M. Hanson, and A. C. Gossard, Science **321**, 229 (2008).
[4] G. Grosso, J. Graves, A. T. Hammack, A. A. High, L. V. Butov, M. Hanson, and A. C. Gossard, Nat. Photon. **3**, 577 (2009).
[5] A. Violante, K. Cohen, S. Lazic, R. Hey, R. Rapaport, and P. V. Santos, New J. Phys. **16**, 033035 (2014).
[6] T. Guenther, C. Lienau, T. Elsaesser, M. Glanemann, V. M. Axt, T. Kuhn, S. Eshlaghi, and A. D. Wieck, Phys. Rev. Lett. **89**, 057401 (2002).
[7] M. K. L. Man, A. Margiolakis, S. Deckoff-Jones, T. Harada, E. L. Wong, M. B. M. Krishna, J. Madeo, A. Winchester, S. Lei, R. Vajtai *et al.*, Nat. Nanotechnol **12**, 36 (2016).
[8] K. F. Mak, C. Lee, J. Hone, J. Shan, and T. F. Heinz, Phys. Rev. Lett. **105**, 136805 (2010).
[9] A. Splendiani, L. Sun, Y. Zhang, T. Li, J. Kim, C.-Y. Chim, G. Galli, and F. Wang, Nano Lett. **10**, 1271 (2010).
[10] G. Wang, A. Chernikov, M. M. Glazov, T. F. Heinz, X. Marie, T. Amand, and B. Urbaszek, Rev. Mod. Phys. **90**, 021001 (2018).
[11] T. Mueller and E. Malic, npj 2D Mater. Appl. **2**, 29 (2018).
[12] M. Kulig, J. Zipfel, P. Nagler, S. Blanter, C. Schüller, T. Korn, N. Paradiso, M. M. Glazov, and A. Chernikov, Phys. Rev. Lett. **120**, 207401 (2018).
[13] F. Cadiz, C. Robert, E. Courtade, M. Manca, L. Martinelli, T. Taniguchi, K. Watanabe, T. Amand, A. C. H. Rowe, D. Paget *et al.*, Appl. Phys. Lett. **112**, 152106 (2018).
[14] C. Jin, E. Y. Ma, O. Karni, E. C. Regan, F. Wang, and T. F. Heinz, Nat. Nanotechnol. **13**, 994 (2018).
[15] F. Rossi and T. Kuhn, Rev. Mod. Phys. **74**, 895 (2002).
[16] Q. Vu, H. Haug, and L. Keldysh, Solid State Commun. **115**, 63 (2000).
[17] K. Siantidis, V. M. Axt, and T. Kuhn, Phys. Rev. B **65**, 035303 (2001).
[18] M. Kira and S. Koch, Prog. Quantum Electron. **30**, 155 (2006).
[19] S. Brem, M. Selig, G. Berghaeuser, and E. Malic, Sci. Rep. **8**, 8238 (2018).
[20] F. Steininger, A. Knorr, T. Stroucken, P. Thomas, and S. W. Koch, Phys. Rev. Lett. **77**, 550 (1996).
[21] M. Herbst, M. Glanemann, V. M. Axt, and T. Kuhn, Phys. Rev. B **67**, 195305 (2003).
[22] B. Pasenow, M. Reichelt, T. Stroucken, T. Meier, and S. W. Koch, Phys. Rev. B **71**, 195321 (2005).
[23] D. Reiter, M. Glanemann, V. M. Axt, and T. Kuhn, Phys. Rev. B **73**, 125334 (2006).
[24] D. Reiter, M. Glanemann, V. M. Axt, and T. Kuhn, Phys. Rev. B **75**, 205327 (2007).
[25] F. Lengers, R. Rosati, T. Kuhn, and D. Reiter, Acta Phys. Pol. A **132**, 372 (2017).
[26] F. Grasselli, A. Bertoni, and G. Goldoni, J. Chem. Phys. **142**, 034701 (2015).
[27] F. Grasselli, A. Bertoni, and G. Goldoni, Phys. Rev. B **93**, 195310 (2016).
[28] D. Bimberg, R. Blachnik, M. Cardona, P. Dean, T. Grave, G. Harbeke, K. Hübner, U. Kaufmann, W. Kress, O. Madelung *et al.*, *Physics of Group IV Elements and III-V Compounds, Landolt Börnstein, New Series*, 1st ed. (Springer, Berlin, 1982), Vol. 17a.
[29] V. M. Axt and S. Mukamel, *Nonlinear Optical Materials* (Springer, New York, 1998), pp. 33–47.
[30] R. J. Bartlett and M. Musiał, Rev. Mod. Phys. **79**, 291 (2007).
[31] V. M. Axt and A. Stahl, Z. Phys. B **93**, 195 (1994).
[32] F. Prengel and E. Schöll, Phys. Rev. B **59**, 5806 (1999).
[33] L. Hufnagel, R. Ketzmerick, T. Kottos, and T. Geisel, Phys. Rev. E **64**, 012301 (2001).
[34] R. Rosati and F. Rossi, Phys. Rev. B **89**, 205415 (2014).
[35] F. Katsch, M. Selig, A. Carmele, and A. Knorr, Phys. Status Solidi B **255**, 1800185 (2018).